Metamorphic records of multiple seismic cycles during subduction

Daniel R. Viete [1*], Bradley R. Hacker [2], Mark B. Allen [3], Gareth G.E. Seward [2], Mark J. Tobin [4], Chris S. Kelley [5], Gianfelice Cinque [5], Andrew R. Duckworth [6]

1. Department of Earth & Planetary Sciences, Johns Hopkins University, Baltimore, MD 21218, USA
2. Department of Earth Science, University of California Santa Barbara, Santa Barbara, CA 93101, USA
3. Department of Earth Sciences, Durham University, Durham, DH1 3LE, UK
4. The Australian Synchrotron, Clayton, VIC 3168, Australia
5. Diamond Light Source, Harwell Science & Innovation Campus, Didcot, OX11 0DE, UK
6. Department of Chemistry, Durham University, Durham, DH1 3LE, UK

Abstract

Large earthquakes occur in rocks undergoing high pressure/low temperature metamorphism during subduction. Rhythmic major-element zoning in garnet is a common product of such metamorphism, and one that must record a fundamental subduction process. Here we show that rhythmic major-element zoning in subduction-zone garnets from the Franciscan Complex, California developed in response to growth–dissolution cycles driven by pressure pulses. Using electron probe microanalysis and novel techniques in Raman and synchrotron Fourier transform infrared microspectroscopy, we demonstrate that at least four such pressure pulses, of magnitude 100–350 MPa, occurred over less than 300,000 years. These pressure magnitude and time scale constraints are most consistent with the garnet zoning having resulted from periodic overpressure development–dissipation cycles, related to pore-fluid pressure fluctuations linked to earthquake cycles. This study demonstrates that some metamorphic reactions can track individual earthquake cycles, and thereby opens new avenues to the study of seismicity.

Introduction

Earthquakes in subduction zones can produce devastating tsunamis (e.g. the 2004 M9.2 Sumatra–Andaman and 2011 M9.0 Tōhoku 'megathrust' earthquakes), and may discharge subducted volatiles (Nakajima et al., 2011; Spandler et al., 2011) and trigger arc magmatism (Davies, 1999; John et al., 2012). Though subduction seismicity can persist to depths > 600 km, it is most frequent and energetic in the uppermost part of the subducting slab, at depths of 30–70 km (Frohlich, 1989; Kirby et al., 1996; Abers et al., 2006; Green et al., 2010). The record of such seismicity might be visible in high pressure/low temperature (H*P*/L*T*) metamorphic rocks recovered from such depths. More so than for other tectonic environments, links between metamorphism and seismicity are proposed for subduction zones. For example, seismicity at anomalous (> 50–70 km) depths in the subduction setting has been related to embrittlement due to metamorphic dehydration reactions and associated pore-fluid pressure development and/or volume change (Green & Houston, 1995; Kirby et al., 1996; Hacker et al., 2003; Preston

et al., 2003; Jung et al., 2004; Nakajima et al., 2013; Schubnel et al., 2013). Geologic records that contribute to our understanding of the mechanisms and magnitude–recurrence rates for subduction seismicity come chiefly from Quaternary tsunami and turbidite deposits (e.g. Adams, 1990; Goldfinger et al., 2003; Nanayama et al., 2003; Cisternas et al., 2005; Monecke et al., 2008; Gràcia et al., 2010), subsidence/uplift histories from tidal wetlands and coral reefs (e.g. Taylor et al., 1990; Nelson et al., 1996), and pseudotachylytes and breccias (e.g. Austrheim & Boundy, 1994; John & Schenk, 2006; Angiboust et al., 2012). Here we show that garnet—one of the more common metamorphic minerals in H*P*/L*T* metamorphic rocks—may provide new insights into earthquake magnitude–recurrence rates.

The blueschist- and eclogite-facies assemblages produced in subduction metamorphism record uniquely low geothermal gradients, typically < 600 °C GPa^{-1}. Subduction metamorphism can be incredibly rapid, in cases involving time scales < 10^4–10^6 yr (Bjørnerud et al., 2002; Camacho et al., 2005; Raimbourg et al., 2007; Dragovic et al., 2012). Rhythmic major-element zoning in garnet is a common feature in H*P*/L*T* metabasic rocks (e.g. Dudley, 1969; García-Casco et al., 2002; Davis & Whitney, 2006; Tsujimori et al., 2006b; Page et al., 2007; Kabir & Takasu, 2010; Meyer et al., 2016), suggesting that it is a manifestation of a common process (or set of processes) in the subduction setting. To explore the nature of these processes and origin of the H*P*/L*T* garnet zoning, we apply several modern and novel techniques to investigate metamorphism and paleoseismicity in the Jurassic Franciscan Complex, California.

Results

Sample CA13-01 is a garnet-bearing eclogite–blueschist from Ring Mountain, Tiburon Peninsula, San Francisco Bay. Sample CA13-05A is a garnet-rich amphibolite from the same locality. Detailed rock descriptions are provided in the Materials and Methods section, however, of particular relevance for the *P*–*T* conditions of metamorphism is the presence of amphibole (glaucophane in CA13-01; Na–Ca amphibole and glaucophane in CA13-05A) and zoisite, and the absence of lawsonite in both samples. Garnets from both rocks contain rutile and quartz inclusions from core to rim (quartz rare at the rim). Thermodynamic modeling of phase equilibria suggests that garnet rim growth occurred at *P*–*T* of 555–585 °C, 1.4–2.0 GPa for CA13-01 and 535–595 °C, 1.2–2.0 GPa for CA13-05A; these estimates are entirely consistent with earlier thermobarometry of the same rocks (Tsujimori et al., 2006a). Whole-rock geochemistry, methods and results for thermodynamic modeling of metamorphic phase equilibria are provided in the Methods and Materials section.

Electron microprobe x-ray count maps were produced for Ca, Fe, Mg and Mn in 6–7 garnets for each of CA13-01 and CA13-05A; examples of Mg and Mn maps are provided in Fig. 1 and all maps are provided in the supplementary material. Complementary quantitative electron microprobe traverses were measured for one garnet from CA13-01 and two garnets from CA13-05A (Fig. 1). The garnets have inclusion-rich cores that are compositionally distinct from inclusion poor mantles/rims (Fig. 1). Oscillatory/rhythmic zoning in both Mg and Mn is apparent in the mantle/rim zone (Fig. 1), but does not correspond to obvious zoning in Ca or Fe (with the exception of bands at the extreme outer edge of garnets from CA13-01). The Mg and Mn zoning

in some garnets incorporate features of zone incursion (embayments), and circumferential pinching and swelling (Fig. 1). All garnets analyzed display systematic asymmetry in the location of relatively steep compositional gradients (Fig. 1). These features are consistent with the major-element zoning being a result of cycles of garnet growth separated by gaps during which there was no growth or there was dissolution, such that the embayments and steep compositional gradients mark garnet growth 'unconformities'. Quantitative Mn traverses (Fig. 1) confirm the asymmetry in the compositional gradients that flank the Mn highs; relatively steep gradients occur on the rim side of Mn highs for sample CA13-01 and on the core side for sample CA13-05A. Rim-side asymmetry (as observed in CA13-01) must involve overgrowth of thin (high-Mn) resorption bands by lower-Mn garnet, whereas core-side asymmetry (as observed in CA13-05A) must involve overgrowth of the 'unconformity' surface by higher-Mn garnet. The two modes presumably reflect different supply/demand scenarios for Mn following garnet dissolution; reactions associated with the rim-side scenario cannot provide a sanctuary for all Mn liberated by garnet dissolution, leading to back-diffusion of Mn into the garnet. Fig. 2 outlines models for the development of the two types of asymmetric zoning as a result of garnet growth–dissolution cycles.

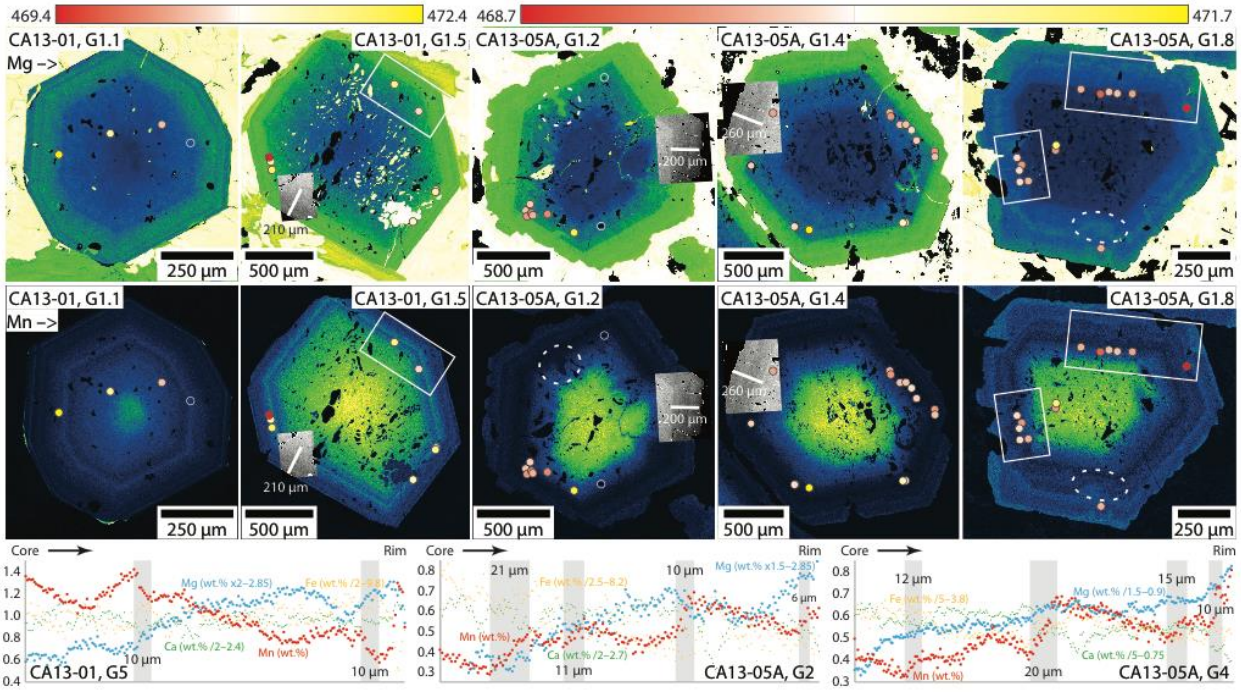

Fig. 1. Color-enhanced wavelength-dispersive spectrometer (WDS) x-ray count maps for Mg (top row of images) and Mn (middle row of images) in garnets from Ring Mountain. Decreasing Mg and Mn content are indicated by yellow–green–blue–black color progression. Spots give location of Raman quartz analyses and are colored according to peak position (±1.5 cm^{-1} about 470.9 cm^{-1} for CA13-01; ±1.5 cm^{-1} about 470.2 cm^{-1} for CA13-05A; see data in Fig. 3d). Transparent spots correspond to partially transparent analyses in Fig. 3d. Spot size indicated is larger than actual ~1 µm spot. White rectangles show notable zones with varying Raman response associated with compositional zoning boundaries (blow-ups provided in the supplementary material). Dashed white ellipses highlight examples of zoning

embayments/incursions. Gray back-scattered electron images indicate locations of quantitative (WDS) electron microprobe traverses at bottom of figure. Regions with steep compositional gradients in the traverses are indicated by vertical gray bands (with length scale indicated).

Franciscan garnet growth–dissolution cycles due to pressure(–temperature) fluctuations

The modal garnet contours for both rocks (see phase assemblage diagrams in Materials and Methods section) suggest that modest changes in *T* or, more so, *P* might have triggered significant garnet production/loss and therefore caused the garnet zoning (i.e. 5–15 vol.% growth/dissolution, relative to starting garnet content, for Δ*T* of 40 °C or Δ*P* of 100 MPa). The gentle slopes in *P*–*T* space for both Mg- and Mn-in-garnet isopleths (see phase assemblage diagrams in Materials and Methods section) are also consistent with rhythmic zoning in Mg and Mn having developed primarily in response to changes in *P*. Garnet zoning is complemented by irregular major-element zoning in glaucophane, omphacite and zoisite in CA13-01, and glaucophane, hornblende and zoisite in CA13-05A. Up-pressure dehydration reactions likely involved breakdown of glaucophane and zoisite to form garnet, jadeite, quartz and H_2O in CA13-01, and breakdown of hornblende and zoisite to form garnet, glaucophane and H_2O in CA13-05A (see Materials and Methods section). In order to test the role of pressure fluctuations in driving garnet growth–dissolution cycles, we performed high-resolution barometry by Raman microspectroscopy on quartz inclusions in garnet, and novel synchrotron Fourier transform infrared (FTIR) microspectroscopy on garnet.

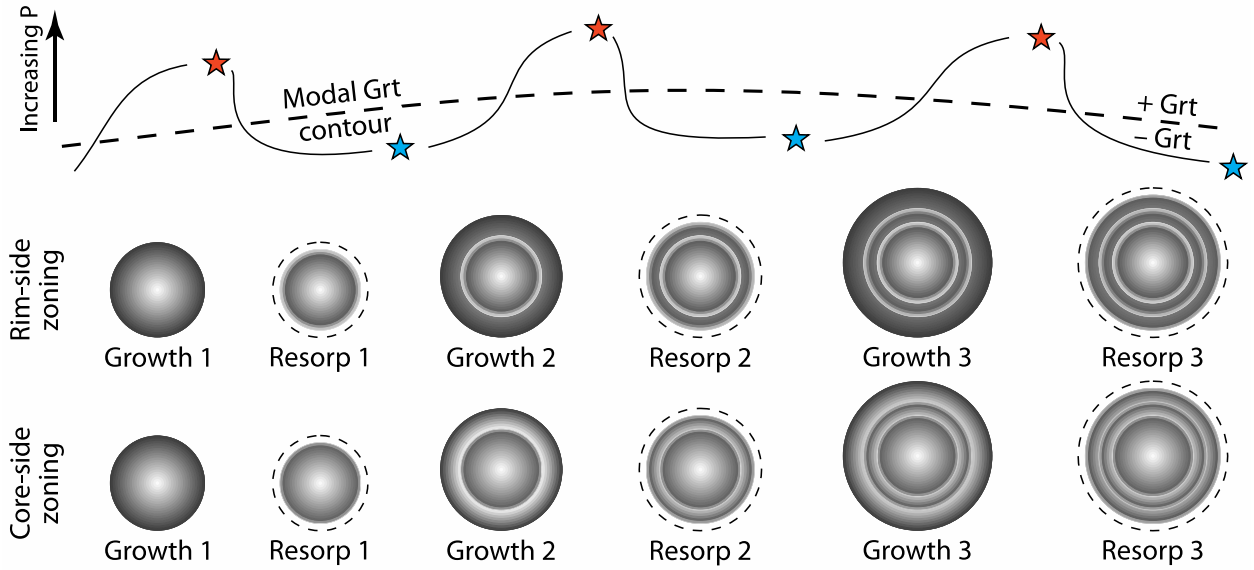

Fig. 2. Conceptual models for development of rim-side (top row of garnets with Mn back-diffusion during resorption) and core-side zoning (bottom row of garnets with no Mn back-diffusion during resorption) by fluctuating garnet stability (growth–resorption cycles) in response to pressure pulses. Blue stars mark onset of undrained conditions at the start of a phase of fluid overpressure development and garnet growth. Orange stars mark full overpressure conditions at the end of a growth phase (immediately prior to an earthquake event), fracturing due to dynamic stresses and relief of overpressure.

Interrogating pressure pulses by spectroscopic methods

Raman barometry uses the pressure dependence of the position of peaks in the Raman spectra for an included mineral to calculate a residual pressure in the inclusion (e.g. Kohn, 2014). This residual pressure results from differential expansion/contraction of host and inclusion following cooling and exhumation and, knowing the thermo-elastic properties of the two minerals, can be used to calculate the *P*–*T* conditions of inclusion overgrowth by host. The properties of quartz and garnet yield an inclusion–host system far more sensitive to overgrowth pressure than temperature, meaning that the quartz-in-garnet system makes a good barometer (e.g. Ashley et al., 2016). The position of (nominal 464 cm^{-1}) quartz Raman A1g-mode peaks were measured in triplicate for 80 quartz-in-garnet inclusions across samples CA13-01 and CA13-05A. Images of quartz inclusions are provided in Fig. 3a–c and detailed methods are provided in the Materials and Methods section. Repeat analyses produced consistent results, yielding 2σ reproducibility of ± 0.3 cm^{-1} (Fig. 3d). With exposed, cracked or compound inclusions (n = 12) excluded, analyses from the two rocks show a significant spread in A1g-mode peak position (4.2–7.2 cm^{-1} above atmospheric for CA13-01, and 3.5–6.5 cm^{-1} above atmospheric for CA13-05A; Fig. 3d). Variable Raman A1g-mode peak position reflects variable residual pressure resulting from different overgrowth pressure. Using the calibration of Schmidt & Ziemann (2000), the elastic model of Guiraud & Powell (2006) and mineral properties recommended by Holland & Powell (2011), the ranges of Raman A1g-mode peak shifts suggest *P* = 1.4–2.1 GPa (median 1.9 GPa) for CA13-01 and *P* = 1.25–1.95 GPa (median 1.5 GPa) for CA13-05A. Spatially, Raman A1g-mode peak position varies by 0.5–1.5 cm^{-1} over garnet radial distances of 10–50 µm and in association with the major-element growth zoning (Fig. 1); we infer that garnet growth–dissolution was associated with fluctuations in metamorphic pressure of magnitude 100–350 MPa.

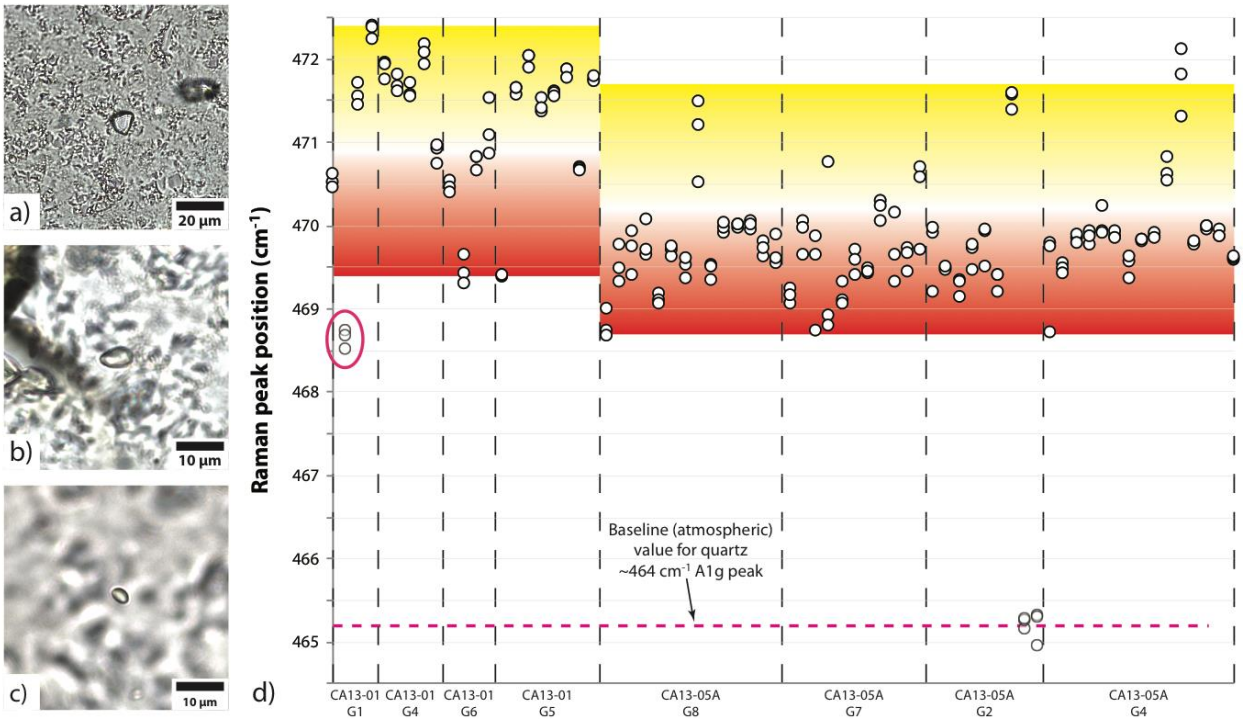

Fig. 3. (a–c) transmitted-light photomicrographs of some analyzed quartz inclusions in garnet. (d) Positions for the nominally 464 cm^{-1} A1g Raman peak for quartz inclusions in garnet from Ring Mountain, analyzed in triplicate. Inclusion circled in pink displays an abnormally low peak position despite lack of evidence that it was exposed during polishing or associated with visible cracks in garnet. Yellow-to-red background coloring for reference to spot colors on garnet x-ray count maps in Fig. 1.

Raman barometry can only be applied where suitable inclusions occur. In order to obtain more complete records of pressure fluctuations during garnet growth/resorption, we also applied an exploratory FTIR absorption spectroscopy for simultaneous garnet barometry and hygrometry. Experimental work has demonstrated a positive relationship between growth pressure and the OH content of pyrope garnet (at mantle pressures; Lu & Keppler, 1997; Withers et al., 1998), and the presence of non-structural (molecular) H_2O in garnet (an impurity) may also act as a proxy for activity (partial pressure) of H_2O (a hygrometer) during garnet growth. Structural OH and molecular H_2O in garnet are associated with independent FTIR spectral peaks within the mid-IR range. Interrogation of the fine major-element zoning in the Franciscan H*P*/L*T* garnets by FTIR spectroscopy requires high-spatial-resolution and high-sensitivity measurement of a component that occurs in extremely low concentrations (< 100 ppm; garnet is nominally anhydrous), meaning that the technique requires an IR source with brightness only offered by synchrotron light. Transmission synchrotron FTIR microspectroscopy was performed on three garnets from CA13-01 and two from CA13-05A, at the Australian Synchrotron and Diamond Light Source, UK. Detailed methods and results are provided in the Materials and Methods section.

Our new, qualitative synchrotron FTIR barometry and hygrometry technique identified regions with steep OH (and to a lesser extent H_2O) concentration gradients in garnet (Fig. 4). These breaks in OH match the locations of the steep compositional gradients that mark garnet growth 'unconformities' (Fig. 4). The correlation is with zoning in Mg and Mn but not Ca, suggesting fluctuations in OH do not simply reflect changes in proportion of the garnet end members that are most commonly hydrated (i.e. grossular/andradite). Regardless of the polarity of Mn change across the 'unconformities' in rim-side (CA13-01) and core-side (CA13-05A) zoning, OH content uniformly shows a sharp rim-side decrease (Fig. 4). This result is consistent with garnet growth (following dissolution) resuming at lower pressure than recorded in the garnet immediately core-side of the growth 'unconformity'—i.e., the synchrotron FTIR results indicate that dissolution was associated with a pressure drop. The synchrotron FTIR results demonstrate the linkage between pressure fluctuations and growth–dissolution cycles proposed in the model for development of the fine-scale, rhythmic compositional zoning in the garnets (Fig. 2). The relationship between OH and H_2O in the garnets is complex, displaying covariance or anti-correlation in some regions, and apparent independence in others. For these rocks, if systematic mechanistic linkages between pressure and fluid activity exist, the synchrotron FTIR approach was unable to resolve them.

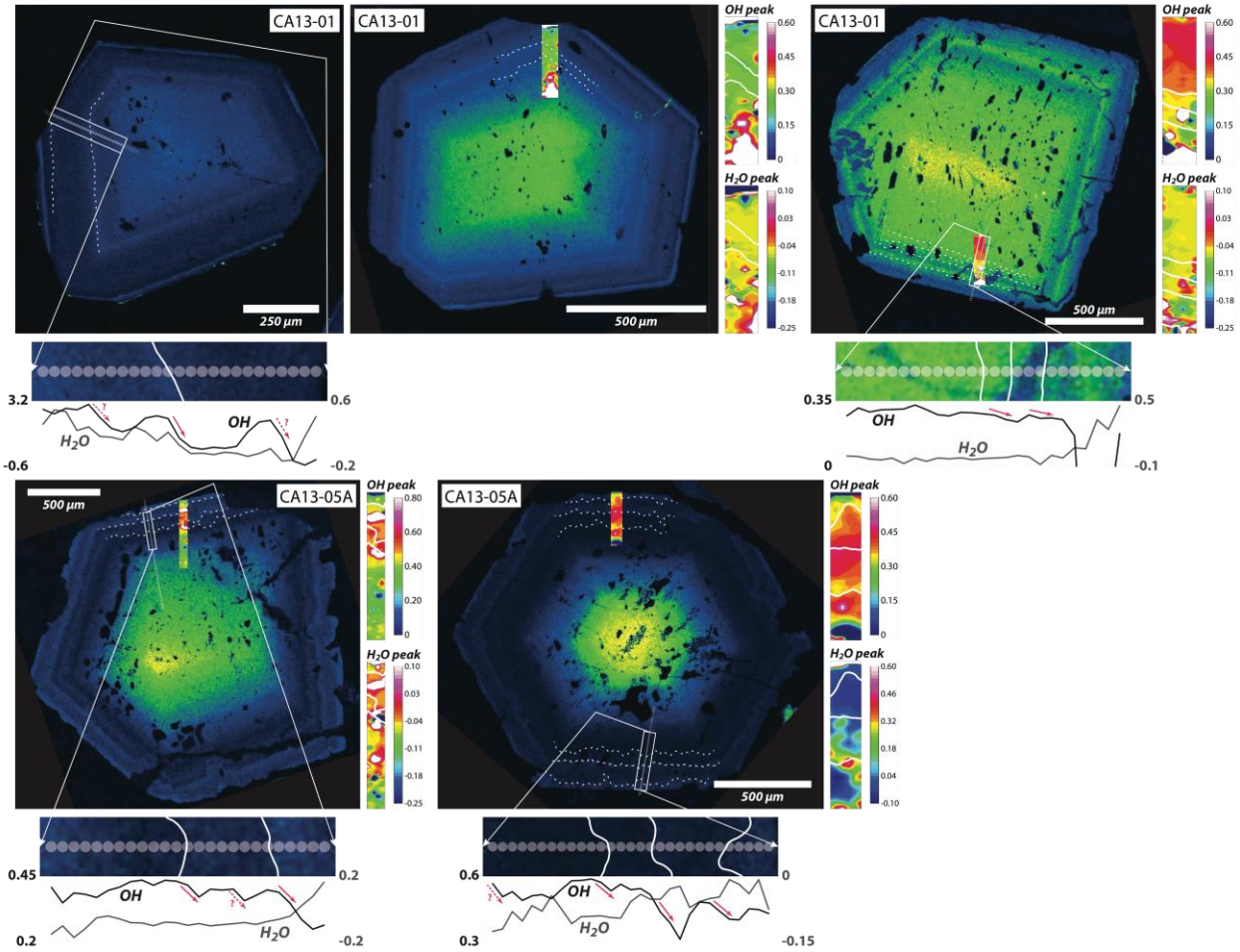

Fig. 4. X-ray count maps for Mn in garnet, synchrotron Fourier transform infrared (FTIR) analysis

1D traverses (bottom of each Mn map) and 2D maps (right of each Mn map) for OH and H_2O. Dashed white lines on Mn maps indicate the position of garnet growth 'unconformities' and correspond to the white lines on the 1D FTIR traverses and 2D FTIR maps. Vertical axis on 1D traverse plots and colors of the 2D FTIR maps correspond to integrated intensity in the 3520–3620 cm^{-1} region for OH (a dimensionless measure of OH abundance) and in the 3350–3450 cm^{-1} region for H_2O (a dimensionless measure of H_2O abundance). Pink arrows on 1D traverse plots indicate regions of decreasing OH in vicinity of garnet growth 'unconformities'.

Short time scales for multiple pressure pulses

The presence of rutile and Ca–Na amphibole in CA13-05A constrain peak T = 535–595 °C at P = 1.2–1.8 GPa, and the presence of glaucophane and absence of chlorite in CA13-01 constrain peak T = 555–585 °C for P = 1.4–1.95 GPa (see metamorphic assemblage diagrams in the Materials and Methods section). The presence of rutile inclusions at the edge of garnet rims is consistent with garnet zoning having developed during the peak-T phase of the metamorphism (T > 550 °C), in agreement with other work on Ring Mountain HP/LT garnets (Tsujimori et al., 2006a), but in contrast to Franciscan HP/LT garnets with retrograde rims from Healdsburg (Page et al., 2007, 2014) and Jenner (Krogh et al., 1994). The absence of lawsonite in both rocks suggests slightly lower maximum pressure than calculated from Raman barometry (< 1.8–2.0 GPa v. 1.9–2.1 GPa). The counter-clockwise P–T path experienced by these rocks involved relatively isobaric refrigeration after peak P–T, followed by monotonic cooling during exhumation (Wakabayashi et al., 1990; Tsujimori et al., 2006a; Page et al., 2007). Preservation of fine-scale diffusion textures in garnet that developed during the peak-T, garnet rim-growth phase of the metamorphism (≤ 10 µm, Fig. 1) means that there was negligible modification during exhumation, despite evidence for a protracted exhumation (cooling) history (Anczkiewicz et al., 2004; Page et al., 2014).

We use an error function approximation to 1D (radial) diffusion [equation of the form $c(x,t) \propto \mathrm{erf}\,(x/\sqrt{4Dt})$, where c, x, t and D are concentration, position, time and diffusivity, respectively] to reproduce Mn diffusion length scales associated with the garnet growth 'unconformities' (≤ 10 µm, Fig. 1), and thereby constrain time scales for formation of the garnet zoning at near-peak metamorphic conditions. This approach assumes an initial step change in Mn concentration associated with the overgrowth/dissolution surface, and no cutting effects or spatial homogenization due to spot size; the calculated estimates are therefore significantly biased toward longer durations. The Mn-in-garnet Arrhenius parameters of Chu & Ague (2015) yield time scales of < 300 kyr for T > 550 °C, P < 2.0 GPa; all of the pressure-driven growth–dissolution cycles must have occurred within this timeframe. Varying the overgrowth P–T from 550 to 590 °C and 1.2 to 2.0 GPa expands the estimate range to < 30–300 kyr. Allowing for Mn-in-garnet Arrhenius parameter values between the most diffusive (Chakraborty & Ganguly, 1992) and the most retentive (Carlson, 2006) published expands the range to < 0.04–1.2 Myr (for mean P–T conditions; T = 570 °C, P = 1.6 GPa). This range is compatible with global subduction speeds (Syracuse & Abers, 2006), indicating that most subducting crust passes through blueschist facies conditions in ~1 Myr.

Discussion

The diffusion length scale data indicate that at least four cycles of pressure fluctuation (of magnitude 100–350 MPa) occurred during H*P*/L*T* metamorphism, net garnet growth length scales of < 100–300 μm and metamorphic time scales very likely << 1 Myr. On the basis of major-element zoning in H*P*/L*T* garnets from Cuba, García-Casco et al. (2002) hypothesized pressure fluctuations of similar magnitude during subduction, relating them to small-scale (physical) exhumation events during prograde metamorphism. The << 1 Myr time scales for garnet zoning development are significantly shorter than hypothesized time scales for multiple burial–exhumation cycles in H*P*/L*T* rocks that have been related to i) 'yo-yo tectonics', involving (local or regional) switches between shortening and extension (e.g. Beltrando et al., 2007; Kabir & Takasu, 2010; Rubatto et al., 2011; Lister & Forster, 2016), ii) exhumation–erosion–deposition–subduction cycles (Wakabayashi et al., 2012), and iii) numerically simulated 'chaotic' mixing as a result of convection within a putative subduction channel (e.g. Gerya et al., 2002; Gerya & Stöckhert, 2006; Blanco-Quintero et al., 2011; Li et al., 2016). These 'lithostatic pressure' models are limited by maximum rates of burial/exhumation; e.g., four 7.5 km (mean magnitude; 225 MPa) burial–exhumation cycles at vertical movement rates approximating tectonic plate velocities—i.e., 30 mm yr^{-1}, as in the subduction convection model of Gerya & Stöckhert, 2006—require at least 2 Myr. It should be noted, however, that modeling of convection within the subduction channel also predicts periodic stalling of particles, yielding more likely time scales of 5–10 Myr per 200–500 MPa physical burial–exhumation cycle (e.g. Gerya & Stöckhert, 2006, Fig. 4, 7, p. 259, 262).

Garnet zoning marks seismic cycles during subduction

Fig. 5 compares time scales for (1) megathrust earthquake recurrence, (2) individual *P* pulses recorded in the H*P*/L*T* garnets of this study, and (3) small-scale physical burial–exhumation cycles, showing that these constraints are most consistent with a seismic cycle origin for the garnet *P* pulse records. We relate rhythmic major-element zoning in the Franciscan garnets to cycles of pore-fluid overpressure development–dissipation, linked to a seismically-induced switch from locally undrained to drained conditions (i.e., dynamic cracking and permeability changes following large earthquakes; see Brenguier et al., 2014; Chaves & Schwartz, 2016).

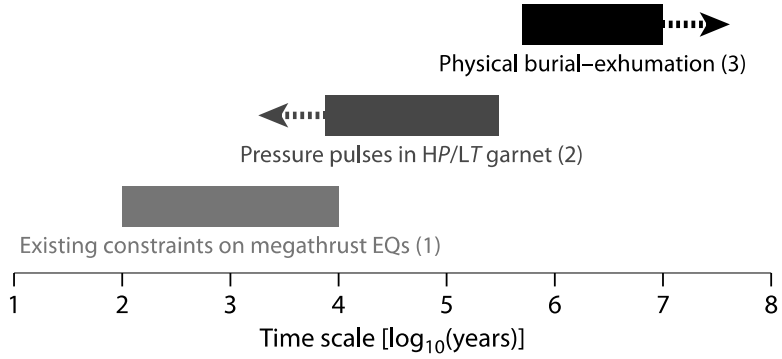

Fig. 5. Time scales for individual cycles relating to: (1) megathrust earthquake (EQ) events from tsunami and turbidite deposits and subsidence/uplift histories; (2) garnet dissolution–growth and associated *P* pulses as recorded in the garnets of this study, and (3) physical burial–exhumation cycles relating to 'yo-yo' tectonics, exhumation–erosion–deposition–subduction cycles or convection within a putative subduction channel. Note, time scales for (2) are maximum values due to bias toward overestimation in the approach used and the possibility that *P* pulses were significantly more numerous than recorded in the garnets (see text).

Though rocks do not typically have unconfined strength greater than 100–200 MPa, the effects of confinement and undrained conditions may allow pore fluid pressure excess (overpressure) to attain more significant values (e.g. Vrijmoed et al., 2009; Padrón-Navarta et al., 2011; Nabelek, 2015). Transient pressure pulses may mark porosity waves that transit the rock volume, or cycles of overpressure development–dissipation linked to subduction-zone seismicity. Porosity waves are only theorized to exist, whereas subduction zone seismicity is an observed phenomenon that has been associated with pore fluid overpressure (e.g. Green & Houston, 1995; Kirby et al., 1996; Hacker et al., 2003; Preston et al., 2003; Jung et al., 2004) and occurs at the depth and location of H*P*/L*T* metamorphism.

Our model for Franciscan garnet zoning invokes widespread rock fracture with passing seismic waves as the trigger for overpressure relief; changes in seismic velocity following megathrust earthquakes have been related to this mechanism of pore-fluid pressure relief (Brenguier et al., 2014; Chaves & Schwartz, 2016). Rock fracture in response to dynamic stresses induced by a large earthquake may also produce a widespread permeability spike. Once fault healing and sealing is complete and conditions again become undrained, feedback between dehydration reactions and increasing metamorphic pressure—due to metamorphic pore-fluid production—can lead to overpressure development and recommenced garnet growth, until dynamic stresses associated with a subsequent large earthquake again cause rock fracture and permeability increase. Not all earthquake events need be recorded and those that were do not need to have been proximal; dynamic stresses and therefore likelihood of local fracturing and overpressure relief would be greatest for the most energetic events (e.g. megathrusts). The model is consistent with our FTIR observation of a decrease in OH across the growth 'unconformity' (Fig. 4). Intimate garnet growth-zone $\delta^{18}O$ variation in the Franciscan garnets (cf. Page et al., 2014) may also be expected for cycles of pore-fluid purging with rock fracture, pressure drop and permeability increase, followed by metamorphic dehydration and overpressure development under undrained conditions. Such work may offer a means to test the fluid overpressure relief (following large earthquakes) model presented here.

Multiple, rapid pressure fluctuations of 100–350 MPa, as observed here in association with garnet zoning, can be achieved by seismic cycles in subduction zones. Large earthquakes have recurrence intervals of 100–10,000 yr (e.g. Taylor, 1990; Goldfinger et al., 2003; Nanayama et al., 2003; Cisternas et al., 2005; Monecke et al., 2008; Gràcia et al., 2010). Though there is some overlap, the H*P*/L*T* garnets studied record frequencies mostly outside of this recurrence range (see Fig. 5). Not every earthquake will cause fracturing and overpressure dissipation; records are only made for those that produced sufficient seismic energy, directed at the rock volume.

This, partnered with potential for garnet dissolution to remove evidence for earlier garnet growth–dissolution cycles (cannibalization of records of *P* pulses), can explain much of the potential discrepancy between time scales for H*P*/L*T* garnet records of *P* pulses and recurrence intervals for large subduction-zone earthquakes (Fig. 5).

We conclude that major-element zoning in the H*P*/L*T* garnets records seismic cycles within the Franciscan subduction zone. Such metamorphic features are common in H*P*/L*T* metamorphic rocks worldwide. In time, geochemical features of H*P*/L*T* garnets (and other minerals) may offer important new insights on the nature of subduction zone (paleo)seismicity, and associations among stress evolution, earthquake magnitude and recurrence, and fluid transport/mobility in the crust.

Materials and Methods

Sample descriptions

The manuscript focuses on two rocks from Ring Mountain, San Francisco Bay, California. Sample CA13-01 [GPS: 37° 55.073’ N, 122° 29.583’ W] is an eclogite–blueschist with 11 vol.% garnet. Sample CA13-05A [GPS: 37° 54.729’ N, 122° 29.122’ W] is a garnet-rich (32 vol.%) amphibolite–blueschist. Garnet populations in both rocks are not uniform, with grain size in each varying from < 0.5 mm to approximately 2 mm across. Both rocks are heterogeneous on a scale of 1–10 mm; CA13-01 has blueschist and eclogite layers, CA13-05A has interfingered amphibolite and blueschist domains. Garnet in CA13-01 is commonly surrounded by phengite, whereas many garnets in CA13-05A are surrounded by clots of chlorite. Mineralogy for each sample is given below. Cross-polarized-light microphotographs are provided in Fig. S1.

(CA13-01) omphacite + garnet + glaucophane + phengite + titanite + zoisite + quartz + rutile
(CA13-05A) hornblende + garnet + glaucophane + zoisite + chlorite + rutile + phengite + omphacite + titanite

Tsujimori et al. (2006a) provided detailed descriptions of three high pressure-low temperature (H*P*/L*T*) rocks from Ring Mountain. Their sample A is incredibly similar in mineralogy and appearance to our CA13-05A. For that sample, Tsujimori et al. (2006a) used petrography, garnet–omphacite–phengite thermobarometry and equilibrium phase assemblage modeling to constrain garnet rim growth to the peak-metamorphic phase, at T = 550–620 °C and P = 2.2–2.5 GPa. Titanite overgrows rutile in both CA13-01 and CA13-05A, and chlorite overgrows garnet in CA13-05A. The Ring Mountain H*P*/L*T* rocks record a counter-clockwise *P*–*T* path, with a metamorphic overprint relating to refrigeration prior to exhumation (Wakabayashi et al., 1990; Tsujimori et al., 2006a). Chlorite and titanite in CA13-01 and titanite in CA13-05A are texturally post-peak metamorphic and grew during the exhumation (and refrigeration) phase of the rock history.

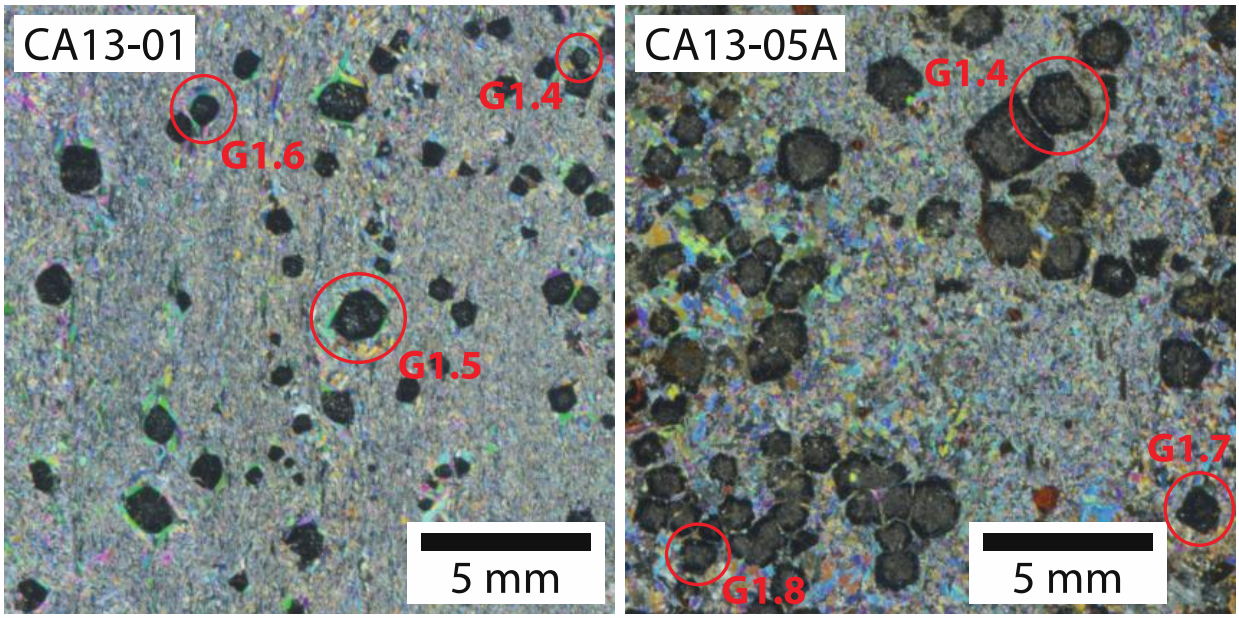

Fig. S1. Cross-polarized-light photomicrographs of samples CA13-01 and CA13-05A. For each rock, some of the garnets mapped for major elements are circled in red.

Electron microprobe methods, mineral chemistry and zoning, and Mn sources

Electron microprobe mapping method and results

Wavelength-dispersive spectrometer (WDS) x-ray count maps for Al, Ca, Fe, Mg and Mn were produced for seven garnets from CA13-01 and six garnets for CA13-05A. Measurements were made simultaneously on the five spectrometers of the Cameca SX 100 electron microprobe in the Department of Earth Science, University of California, Santa Barbara; Al, Ca, Fe, Mg and Mn measurements were made on TAP, LPET, LLIF, LTAP and LLIFF crystals, respectively. Run conditions were 15 keV and 200 nA, and pixel dwell times were 50 ms for all maps except for CA13-01 garnet 2.3, which used 100 ms. Mapping resolution was 2–5 µm, depending on the size of the garnet, and uniform in x and y. Color overlayed maps for all garnets are provided at the end of this document.

Electron microprobe quantitative analysis method and results

Quantitative WDS analyses were produced for three radial garnet traverses (n = 670), a cluster of zoned zoisites from each of CA13-01 and CA13-05A (n = 24), and selected additional minerals from each sample (n = 36). All analyses were performed on the JEOL JXA 8600 electron microprobe in the Department of Earth & Planetary Sciences, Johns Hopkins University. Calibration used multiple natural reference materials. Garnet traverses were run at 15 keV and 40 nA, and used a 1 µm spot size at 1 µm centers and 30 s on-peak and 10 s background counting times. All other analyses were run at 15 keV and 20 nA, and used a 5 µm spot size and 30 s on-peak and 15 s background counting times.

Results for the radial garnet traverses are provided in Fig. 1. Compositions of typical examples of minerals from CA13-01 and CA13-05A are provided in Tables S1 and S2. The subsequent section discusses mineral chemical variability and zoning. All quantitative electron microprobe results are provided in a separate supplementary file.

Table S1. Stoichiometric mineral compositions for CA13-01, based on assumed number of oxygen atoms shown. Note, Fe in zoisite was assumed 100% Fe^{3+}, Fe in all other minerals was assumed 100% Fe^{2+}. Gln = glaucophane; Omph = omphacite; Phe = phengite; Zo = zoisite.

	CA13-01				
	Gln	Omph	Phe	Zo 1	Zo 2
Si	7.99	2.02	3.49	2.91	2.92
Ti	-	-	0.01	0.01	-
Al	1.69	0.36	1.97	2.41	2.25
Cr	-	-	-	-	-
Fe	1.15	0.22	0.19	0.50	0.62
Mn	-	-	-	-	0.01
Mg	2.21	0.44	0.39	0.01	-
Ca	0.15	0.51	-	1.79	1.72
Na	1.87	0.46	0.03	-	-
K	-	-	0.87	-	-
O	23	6	11	12.5	12.5
Al/(Al+Si)	0.17	0.15	0.36	0.45	0.44
Fe/(Fe+Al)	0.41	0.38	0.09	0.17	0.21
Fe/(Fe+Mg)	0.34	0.34	0.33	-	-
Na/(Na+Ca)	0.93	0.48	-	-	-
Na/(Na+K)	-	-	0.04	-	-
Total oxides	97.5	100.6	94.5	96.3	97.6

Table S2. Stoichiometric mineral compositions for CA13-05A, based on assumed number of oxygen atoms shown. Note, Fe in zoisite was assumed 100% Fe^{3+}, Fe in all other minerals was assumed 100% Fe^{2+}. Hbl = hornblende; Gln = glaucophane; Chl = chlorite; Zo = zoisite; Aln = allanite.

	CA13-05A						
	Hbl 1	Hbl 2	Gln	Chl	Zo 1	Zo 2	Aln
Si	7.29	6.92	7.85	2.97	2.91	2.85	2.94
Ti	0.02	0.03	0.01	0.01	0.01	0.06	0.01
Al	1.24	1.91	1.77	2.32	2.41	2.09	2.01
Cr	-	-	-	-	-	-	-
Fe	1.56	1.57	1.30	1.84	0.51	0.73	0.87
Mn	0.02	0.01	0.01	0.02	0.01	0.02	0.02
Mg	3.00	2.67	2.21	2.68	-	-	-
Ca	1.50	1.47	0.12	-	1.77	1.70	1.40
Na	0.82	0.93	1.98	-	-	-	-
K	0.04	0.08	-	0.01	-	-	-
O	23	23	23	14	12.5	12.5	12.5
Al/(Al+Si)	0.15	0.22	0.18	0.44	0.45	0.42	0.41
Fe/(Fe+Al)	0.56	0.45	0.42	0.44	0.17	0.26	0.30
Fe/(Fe+Mg)	0.34	0.37	0.37	0.41	-	-	-
Na/(Na+Ca)	0.35	0.39	0.94	-	-	-	-
Na/(Na+K)	0.95	0.92	-	-	-	-	-

Total oxides	97.1	98.9	97.1	86.1	96.7	97.2	81.0

Solid solution, mineral zoning and Mn sources

Quantitative analyses demonstrate variability in composition for all minerals analyzed. Zoning in individual minerals can capture the full range of compositional variation observed for omphacite and zoisite in CA13-01, and hornblende and zoisite in CA13-05A. Amphiboles from CA13-01 are glaucophane, with Na/(Na + Ca) ≈ 94% (Fig. S2a). One population of amphibole in CA13-05A has similar glaucophane chemistry, whereas the other is a hornblende, with composition between actinolite and pargasite (Fig. S2a). Clinopyroxene in CA13-01 is omphacite, with 39–53 mol.% jadeite (Fig. S2b). Chlorite in CA13-05A varies in composition, with Fe/(Fe + Mg) in the range 37–45% and Si increasing with Fe (Fig. S2c). White mica in CA13-01 also varies in composition, potentially defining two (phengitic) compositional arrays between celadonite and muscovite/paragonite (Fig. S2d). Phengite in CA13-01 has Si content 3.34–3.54 p.f.u.

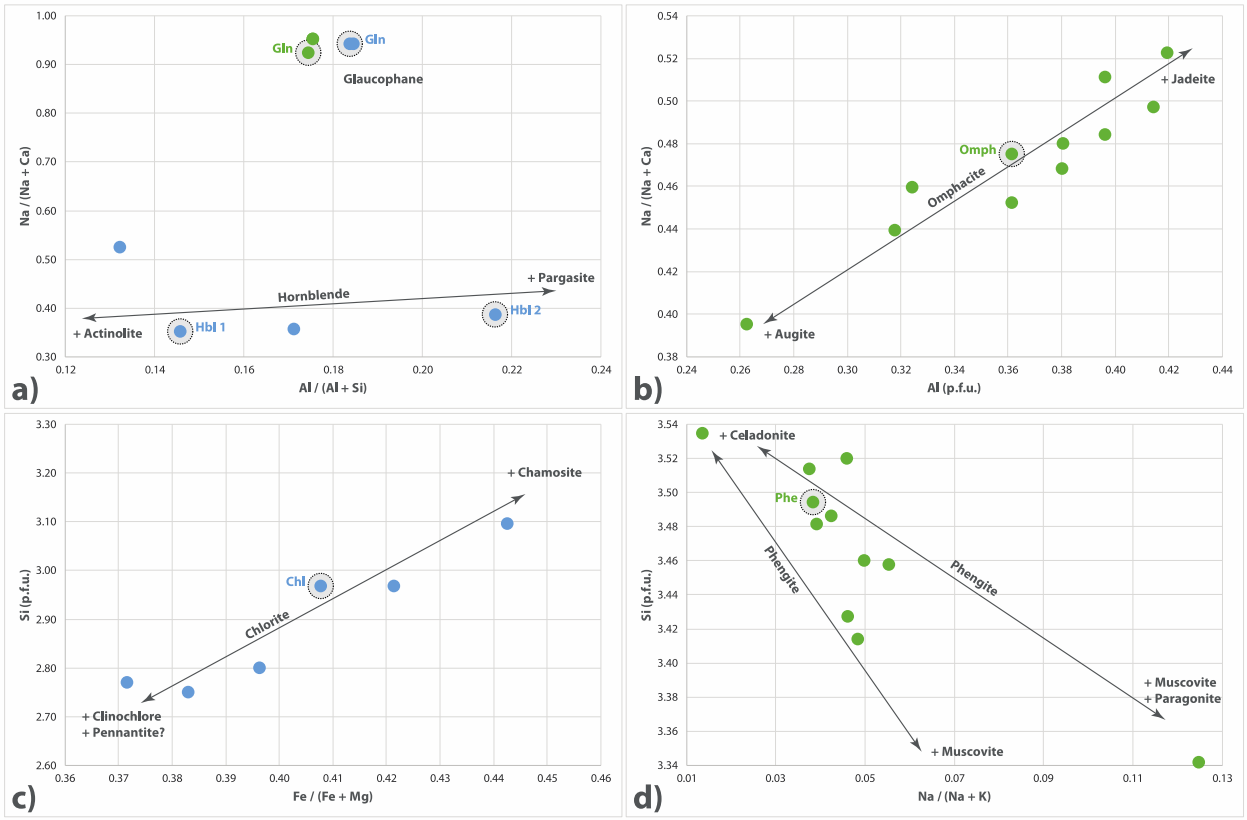

Fig. S2. Plots showing solid solution for (a) amphibole, (b) clinopyroxene, (c) chlorite, and (d) white micas. Green data are for CA13-01, blue data for CA13-05A. Circled points are those whose geochemistry is given in Tables S1 and S2.

The compositional arrays and populations of Fig. S2 are reflected in back-scattered electron (BSE) zoning in amphibole and omphacite. In addition, zoisite has fine-scale, oscillatory BSE zoning (Fig. S3). The zoning principally relates to Fe^{3+} and Al substitution in the epidote–zoisite

solid solution (Fig S3; Tables S1 and S2), but also maps with Mn content, particularly in CA13-05A (Fig S3). Complementary Mn zoning in zoisite to that observed in garnet (see Results section) suggests zoisite growth may have partially balanced garnet dissolution (and vice versa). This observation is consistent with parallelism of modal garnet and zoisite contours (Fig. S4). Garnet breakdown in the presence of H_2O produces zoisite only if other reactants are able to balance the remaining chemistry. Garnet growth–dissolution reactions that mark *P* pulses (seismic loading–rupture cycles) may have involved garnet, jadeite, quartz and H_2O to yield Na amphibole and zoisite (and vice versa) in CA13-05C, and garnet, Na amphibole and H_2O to yield Na–Ca amphibole and zoisite (and vice versa) in CA13-01.

The predicted garnet-growth to zoisite-dissolution ratio for an isothermal, 250 MPa *P* pulse starting at *T* = 570 °C, *P* = 1.55 GPa is greater for CA13-01 (5:1.25) than CA13-05A (9:4) (Fig. S4). The Mn-in-garnet to Mn-in-zoisite ratio is also greater for CA13-01 (approx. 1.0:0.1) than CA13-05A (approx. 0.5:0.2). Hornblende, a product of garnet breakdown in CA13-05A, has up to 0.11 wt.% Mn. More accommodating hosts for Mn liberated during breakdown of garnet in CA13-05A may account for limited Mn back-diffusion during garnet dissolution in CA13-05A (relative to CA13-01) and thus development of core-side rather than rim-side zoning in those garnets (see Fig. 2).

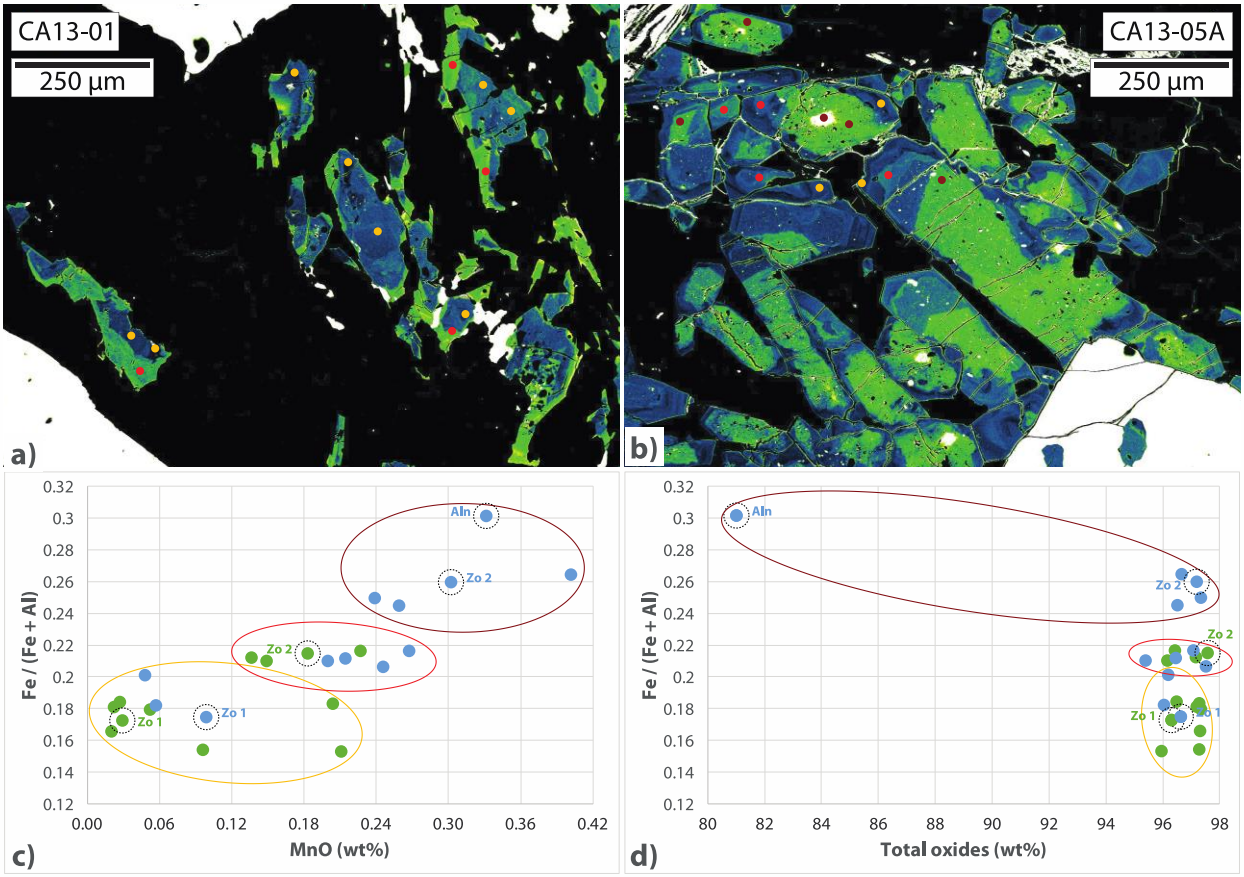

Fig. S3. (a and b) color-overlayed BSE maps for zoisite in CA13-01 and CA13-05A, highlighting fine-scale oscillatory zoning. (c) shows a positive correlation between Fe/(Fe + Al) and MnO in

zoisite. (d) shows one analysis with lower oxide totals than all others; an allanite that contains a high proportion of trace elements not analyzed for. Green data are for CA13-01, blue data for CA13-05A. Yellow, red and maroon groupings match the color of analysis spots and low to high BSE response, respectively, in the maps. Spots on maps are three times larger than actual analyses.

Whole-rock geochemistry, and thermodynamic modeling method and results

Whole-rock geochemistry

Approximately 20 g of fresh and representative material from each of CA13-01 and CA13-05A was ground to powder in a tungsten carbide ring-and-puck mill. Lithium borate fused glass beads were prepared for analysis with a sample (powder) to flux ratio of 1:5. Whole-rock geochemical analyses for major elements were performed on the PANalytical Axios Advanced x-ray fluorescence (XRF) spectrometer in the Department of Geology, University of Leicester. Results from the XRF work are provided in Table S3.

Table S3. Whole-rock geochemistry determined by XRF (values in wt.%).

	SiO_2	TiO_2	Al_2O_3	Fe_2O_3	MnO	MgO	CaO	Na_2O	K_2O	P_2O_5	SO_3	LOI	Total
CA13-01	48.09	1.53	15.78	9.90	0.19	5.38	10.74	3.49	1.54	0.12	<0.002	1.26	98.02
CA13-05A	40.85	2.84	16.43	17.23	0.35	6.36	12.53	1.11	0.13	0.10	0.112	1.28	99.32

Perple_X thermodynamic modeling of metamorphic phase equilibria

Thermodynamic modeling of metamorphic phase equilibria was performed in the MnNCKFMASHT system, using the whole-rock compositions in Table S3. Whole-rock compositions were considered in preference to porphyroblast-subtracted compositions as the modeling was performed to interrogate sensitivity of garnet content (and growth or dissolution) to changes in *P*–*T*; a highly responsive, porphyroblast-involved system is assumed. For each model, the rock was considered saturated in H_2O (set to 10 wt.%) and Fe determined from XRF was recalculated to 100% ferrous (FeO); the only mineral in the rock with significant Fe^{3+} is epidote and that accounts for only a limited proportion of the zoisite (see Fig. S3). Modeling used version 6.6.6 of the Perple_X program (Connolly, 2005, 2009), the 2004 update of the thermodynamic dataset of Holland & Powell (1998), and solution models for amphibole (Wei & Powell, 2003; White et al., 2003), biotite (Powell & Holland, 1999; White et al., 2000), chlorite (Holland et al., 1998), clinopyroxene (Green et al., 2007; Diener & Powell, 2012), feldspar (Fuhrman & Lindsley, 1998), fluid (Connolly & Trommsdorf, 1991), garnet (White et al., 2000), ilmenite (White et al., 2000), melt (Holland & Powell, 2001; White et al., 2001) and white mica (Coggon & Holland, 2002; Auzanneau et al., 2010). Modeling was performed in the range *T* = 525–625 °C and *P* = 1.4–2.4 GPa for CA13-01, and *T* = 525–625 °C and *P* = 1.2–2.2 GPa for CA13-05A. Fig. S4 shows metamorphic assemblage diagrams for both samples, with modal abundance contours for both garnet and zoisite (Fig. S4a and b) and Mg garnet (pyrope) and Mn garnet (spessartine) (Fig. S4c and d) overlain.

Raman thermobarometry method and results

Raman spectroscopy was performed on quartz inclusions in garnet using a Horiba Jobin–Yvon LabRAM HR Raman microscope in the Department of Chemistry, Durham University. All analyses used an 1800 grid (1800 grooves mm^{-1} grating), centered at 470 cm^{-1}. For each quartz inclusion analysis, a 100x confocal objective lens was used to focus the 632.8 nm (red) HeNe laser to a spot size of 1 µm, centered in the inclusion. Quartz inclusions were inspected for exposure and/or cross-cutting cracks, and analysed in triplicate (three measurements in separate sessions). Precise peak positions were obtained by fitting of Lorenzian curves to the nominal 464 cm^{-1} A1g-mode quartz Raman peak (for unknowns), using the software package Igor Pro. Curve fitting to the nominal 464 cm^{-1} A1g-mode peak in quartz used the portion of the spectrum 12 grid points either side of the maximum intensity position, representing a total range of ~7.6 cm^{-1}.

Instrument drift due to internal temperature equilibration was corrected for by quasi-hourly (duplicate) measurement of a pure sulfur Raman spectroscopy standard. Analyses on sulfur standards used a 50x objective and the same 632.8 nm (red) HeNe laser, focused to the position within the homogeneous standard that produced maximum spectrum intensity. For the sulfur standard spectra, curve fitting to the nominal 384.1 cm^{-1} mode peak used the portion of the spectra eight grid points either side of the maximum intensity position (total range of ~5.1 cm^{-1}), a Lorenzian form and the software package Igor Pro. Drift in the position of the nominal 384.1 cm^{-1} sulfur peak during each Raman session was characterized by an equation of the form [$y = -A \exp(-t / b) + c$], where y is the measured peak position minus the nominal 384.1 cm^{-1} value, t is time since the first measurement of the session, A and b are shape constants and c is a vertical shift constant. Values of A, b and c for each session were calculated from a fit to the sulfur data for that session. Following correction for instrument drift at the time of measurement, unknowns were found to have an overall 2σ reproducibility of ± 0.3 cm^{-1} for the peak position of the nominal 464 cm^{-1} A1g-mode quartz Raman peak, despite measurements being made on separate days (see Results section and Fig. 3). Uncorrected spectra (with time stamps) for both quartz inclusions (unknowns) and sulfur standards are available at https://doi.org/10.7281/T1/SP6KO3.

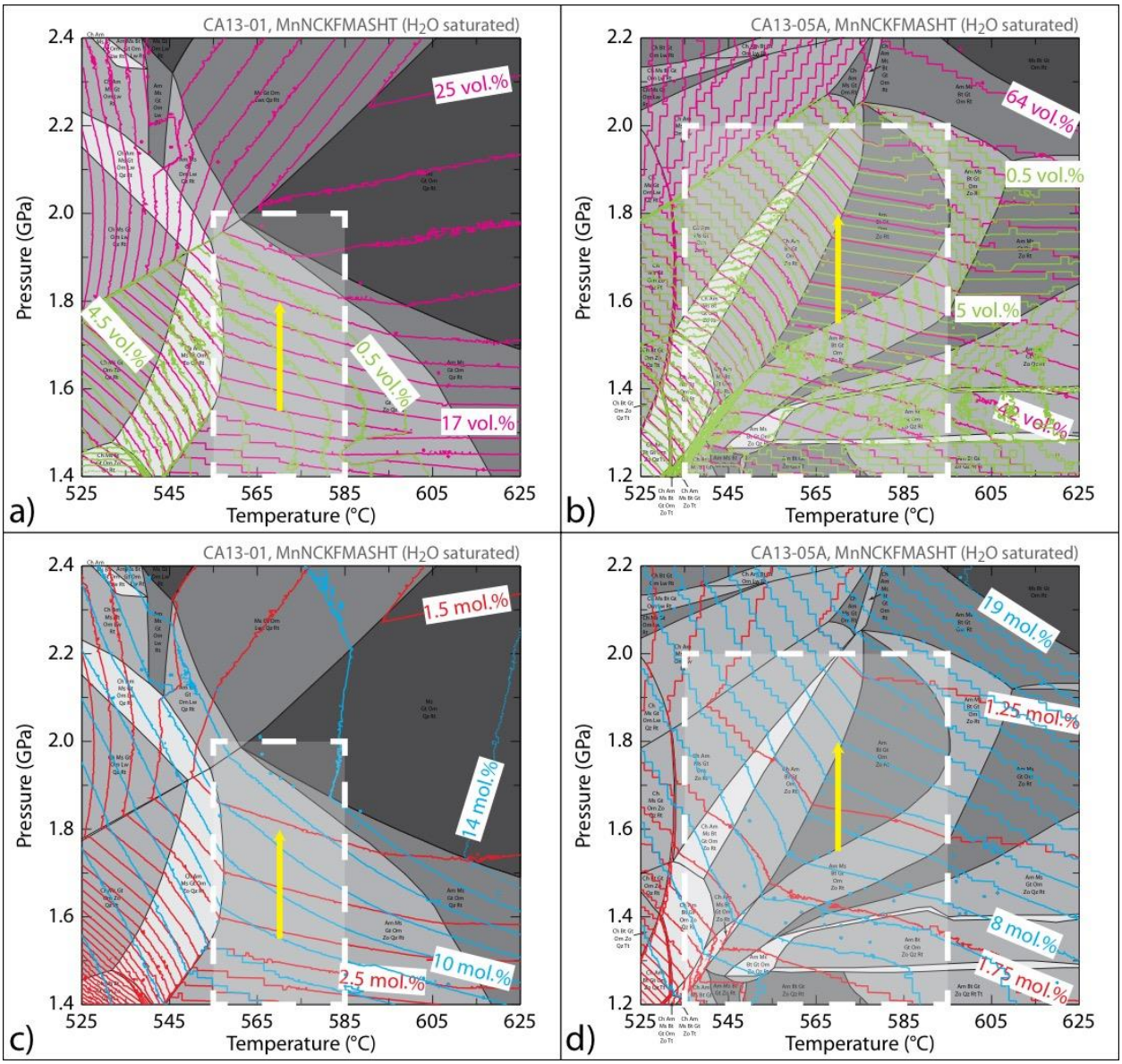

Fig. S4. MnNCKFMASHT metamorphic assemblage diagrams for (a and c) CA13-01 and (b and d) CA13-05A. Phase assemblage fields and labels redrafted from the Perple_X output. White dashed box indicates approximate equilibrium *P*–*T* range of the peak-metamorphic assemblage in each rock. Green and pink contours in a and b are for modal zoisite and garnet, respectively; contour intervals of 0.5 vol.% used for zoisite, and 1 and 2 vol.% for garnet in CA13-01 and CA13-05A, respectively. Note significant congruence between zoisite and garnet contours, suggesting a metamorphic relationship between the phases (i.e. dissolution of one partially accommodates growth of the other). Yellow arrow shows 250 MPa isothermal *P* increase (starting at *T* = 570 °C, *P* = 1.55 GPa), associated with an absolute gain of 5 vol.% garnet and loss of 1.25 vol.% zoisite for CA13-01, and an absolute gain of 9 vol.% garnet and loss of 4 vol.% zoisite for CA13-05A. Blue and red contours in c and d are for proportion of Mg garnet (pyrope) and Mn garnet (spessartine), respectively; contour intervals of 1 mol.% used for pyrope and 0.25 mol.% for spessartine.

Calculation of overgrowth *P* and *T* used the MATLAB QuiBCalc program of Ashley et al. (2014), quartz Raman calibration of Schmidt & Ziemann (2000), mineral properties compiled in Powell & Holland (2011) and the elastic model of Guiraud & Powell (2006). Properties of garnet were calculated by linear interpolation between almandine, grossular, pyrope and spessartine, using respective molar ratios of 59:26:11:4 for CA13-01 and 56:28:15:1 for CA13-05A. These garnet compositions match microprobe-determined rim compositions for the garnets (see Fig. 1). For the same Raman shifts, the elastic model of Zhang (1998) yields *P* estimates that are systematically higher, by 100–200 MPa.

Synchrotron Fourier transform infrared (FTIR) method and results

Microanalyses made at the Diamond Light Source were performed in transmission mode, with spectral resolution of 16 cm^{-1} and phase resolution of 128, using a 700–3200 cm^{-1} window. Analyses used a 36x objective and 10 x 10 µm square slit size defining the detected area at the sample. Each spectrum was produced from 3000 scans and backgrounds were collected prior to each traverse. Four traverses were run radially across the zoning at the garnet edge, using 10 µm centers; n = 39 for CA13-01 G1T2, n = 35 for CA13-01 G2T1, n = 76 for CA13-05A G1T1, n = 46 for CA13-05A G2T1. Microanalyses made at The Australian Synchrotron were also performed in transmission mode, with spectral resolution of 16 cm^{-1} and phase resolution of 128, using a 700–3200 cm^{-1} window. Analyses again used a 36x objective, but a circular spot size of 11.6 µm. Each spectrum was produced from 512 scans, and backgrounds were collected prior to each map. The 2D maps approximated 1D radial traverses, forming elongate grids with dimension 6 x 44 (n = 264) for CA13-01 G1T3, 5 x 39 (n = 195) for CA13-01 G2T2, 6 x 45 (n = 270) for CA13-01 G3T1, 6 x 81 (n = 486) for CA13-05A G1T2, 6 x 48 (n = 288) for CA13-05A G2T2. All line maps used 12 µm centers in the 'circumferential' direction and 6 µm centers (approximate 2x oversampling) in the radial direction. CA13-01 garnet 2, map G2T2, collected at The Australian Synchrotron, experienced irrecoverable issues with background correction.

In total, analyses were performed in transmission mode on three garnets from a clean, ~225 µm-thick wafer of sample CA13-01 and two garnets from a clean, ~280 µm-thick wafer of sample CA13-05A. Relative OH and H_2O contents were calculated from the integrated intensity of the background-subtracted spectra in the 3520–3620 cm^{-1} and 3350–3450 cm^{-1} mid-IR regions, respectively. Integrated intensity calculations were performed with the OPUS software package, using a linear integration baseline. Processed data for the integrated intensities of OH and H_2O in the five garnets analyzed by synchrotron FTIR spectroscopy are provided in Fig. 4. Raw data (as OPUS files) for all synchrotron FTIR analyses are available at https://doi.org/10.7281/T1/SP6KO3.

References

Abers, G.A., van Keken, P.E., Kneller, E.A., Ferris, A. & Stachnik, J.C., 2006. The thermal structure of subduction zones constrained by seismic imaging: implications for slab dehydration and wedge flow. *Earth & Planetary Science Letters* **241**, 387–397.

599 Adams, J., 1990. Paleoseismicity of the Cascadia subduction zone: evidence from turbidites off
600 the Oregon–Washington margin. *Tectonics* **9**, 569–583.
601 Anczkiewicz, R., Platt, J.P., Thirlwall, M.F. & Wakabayashi, J., 2004. Franciscan subduction off to
602 a slow start: evidence from high-precision Lu–Hf garnet ages on high-grade blocks. *Earth &*
603 *Planetary Science Letters* **225**, 147–161.
604 Angiboust, S., Agard, P., Yamato, P. & Raimbourg, H., 2012. Eclogite breccias in a subducted
605 ophiolite: a record of intermediate-depth earthquakes?. *Geology* **40**, 707–710.
606 Ashley, K.T., Steele-MacInnis, M. & Caddick, M.J., 2014. *QuIB Calc*: a MATLAB® script for
607 geobarometry based on Raman spectroscopy and elastic modeling of quartz inclusions in
608 garnet. *Computers & Geosciences* **66**, 155–157.
609 Ashley, K.T., Steele-MacInnis, M., Bodnar, R.J. & Darling, R.S., 2016. Quartz-in-garnet inclusion
610 barometry under fire: reducing uncertainty from model estimates. *Geology* **44**, 699–702.
611 Auzanneau, E., Schmidt, M.W., Vielzeuf, D. & Connolly, J.A.D., 2010. Titanium in phengite: a
612 geobarometer for high temperature eclogites. *Contributions to Mineralogy & Petrology* **159**,
613 1–24.
614 Austrheim, H. & Boundy, T.M., 1994. Pseudotachylytes generated during seismic faulting and
615 eclogitization of the deep crust. *Science* **265**, 82–83.
616 Beltrando, M., Hermann, J., Lister, G.S. & Compagnoni, R., 2007. On the evolution of orogens:
617 pressure cycles and deformation mode switches. *Earth & Planetary Science Letters* **256**, 372–
618 388.
619 Brenguier, F., Campillo, M., Takeda, T., Aoki, Y., Shapiro, N.M., Briand, X., Emoto, K. & Miyake,
620 H., 2014. Mapping pressurized volcanic fluids from induced crustal seismic velocity drops.
621 *Science* **345**, 80–82.
622 Blanco-Quintero, I.F., García-Casco, A. & Gerya, T.V., 2011. Tectonic blocks in serpentinite
623 mélange (eastern Cuba) reveal large-scale convective flow of the subduction channel. *Geology*
624 **39**, 79–82.
625 Bjørnerud, M.G., Austrheim, H. & Lund, M.G., 2002. Processes leading to eclogitization of
626 subducted and tectonically buried crust. *Journal of Geophysical Research B* **107**, 2252.
627 Camacho, A., Lee, J.K.W., Hensen, B.J. & Braun, J., 2005. Short-lived orogenic cycles and the
628 eclogitization of cold crust by spasmodic hot fluids. *Nature* **435**, 1191–1196.
629 Carlson, W.D., 2006. Rates of Fe, Mg, Mn, and Ca diffusion in garnet. *American Mineralogist* **91**,
630 1–11.
631 Chakraborty, S. & Ganguly, J., 1992. Cation diffusion in aluminosilicate garnets: experimental
632 determination in spessartine–almandine diffusion couples, evaluation of effective binary
633 diffusion coefficients, and applications. *Contributions to Mineralogy & Petrology* **111**, 74–86.
634 Chaves, E.J. & Schwartz, S.Y., 2016. Monitoring transient changes within overpressured regions
635 of subduction zones using ambient seismic noise. *Science Advances* **2**, e1501289.
636 Chu, X. & Ague, J.J., 2015. Analysis of experimental data on divalent cation diffusion kinetics in
637 aluminosilicate garnets with application to timescales of peak Barrovian metamorphism,
638 Scotland. *Contributions to Mineralogy & Petrology* **170**, 25.
639 Cisterna, M., Atwater, B.F., Torrejón, F., Sawai, Y., Machuca, G., Lagos, M., Eipert, A., Youlton,
640 C., Salgado, I., Kamataki, T., Shishikura, M., Rajendran, C.P., Malik, J.K., Rizal, Y. & Husni, M.,
641 2005. Predecessors of the giant 1960 Chile earthquake. *Nature* **437**, 404–407.

642 Coggon, R. & Holland, T.J.B., 2002. Mixing properties of phengitic micas and revised garnet–
643 phengite thermobarometers. *Journal of Metamorphic Geology* **20**, 683–696.
644 Connolly, J.A.D., 2005. Computation of phase equilibria by linear programming: a tool for
645 geodynamic modeling and its application to subduction zone decarbonation. *Earth &*
646 *Planetary Science Letters* **236**, 524–541.
647 Connolly, J.A.D., 2009. The geodynamic equation of state: what and how. *Geochemistry,*
648 *Geophysics, Geodynamics* **10**, Q10014.
649 Connolly, J.A.D. & Trommsdorff, V., 1991. Petrogenetic grids for metacarbonate rocks —
650 pressure–temperature phase-diagram projection for mixed-volatile systems. *Contributions to*
651 *Mineralogy & Petrology* **140**, 353–362.
652 Davies, J.H., 1999. The role of hydraulic fractures and intermediate-depth earthquakes in
653 generating subduction-zone magmatism. *Nature* **398**, 142–145.
654 Davis, P.B. & Whitney, D.L., 2006. Petrogenesis of lawsonite and epidote eclogite and
655 blueschist, Sivrihisar Massif, Turkey. *Journal of Metamorphic Geology* **24**, 823–849.
656 Diener J.F.A. & Powell, R., 2012. Revised activity–composition models for clinopyroxene and
657 amphibole. *Journal of Metamorphic Geology* **30**, 131–142.
658 Dragovic, B., Samanta, L.M., Baxter, E.F. & Selverstone, J., 2012. Using garnet to constrain the
659 duration and rate of water-releasing metamorphic reactions during subduction: An example
660 from Sifnos, Greece. *Chemical Geology* **314–317**, 9–22.
661 Dudley, P.P., 1969. Electron microprobe analyses of garnet in glaucophane schists and
662 associated eclogites. *American Mineralogist* **54**, 1139–1150.
663 Frohlich, J.H., 1989. The nature of deep-focus earthquakes. *Annual Reviews in Earth & Planetary*
664 *Sciences* **17**, 227–254.
665 Fuhrman, M.L. & Lindsley, D.H., 1998. Ternary-feldspar modeling and thermometry. *American*
666 *Mineralogist* **73**, 201–215.
667 García-Casco, A., Torres-Roldán, R.L., Millán, G., Monié, P. & Schneider, J., 2002. Oscillatory
668 zoning in eclogitic garnet and amphibole, Northern Serpentinite Melange, Cuba: a record of
669 tectonic instability during subduction?. *Journal of Metamorphic Geology* **20**, 581–598.
670 Gerya, T.V. & Stöckhert, B., 2006. Two-dimensional numerical modelling of tectonic and
671 metamorphic histories at active continental margins. *International Journal of Earth Sciences*
672 **95**, 250–274.
673 Gerya, T.V., Stöckhert, B. & Perchuk, A., 2002. Exhumation of high-pressure metamorphic rocks
674 in a subduction channel: a numerical simulation. *Tectonics* **21**, 1056.
675 Goldfinger, C., Nelson, C.H., Johnson, J.E. & The Shipboard Scientific Party, 2003. Holocene
676 earthquake records from the Cascadia subduction zone and northern San Andreas fault based
677 on precise dating of offshore turbidites. *Annual Reviews in Earth & Planetary Sciences* **31**,
678 555–577.
679 Gràcia, E., Vizcaino, A., Escutia, C., Asioli, A., Rodés, Á., Pallàs, R., Garcia-Orellana, J., Lebreiro, S.
680 & Goldfinger, C., 2010. Holocene earthquake record offshore Portugal (SW Iberia): testing
681 turbidite paleoseismology in a slow-convergence margin. *Quaternary Science Reviews* **29**,
682 1156–1172.
683 Green, E., Holland, T.J.B. & Powell, R., 2007. An order–disorder model for omphacitic pyroxenes
684 in the system jadeite–diopside–hedenbergite–acmite, with application to eclogitic rocks.
685 *American Mineralogist* **92**, 1181–1189.

686 Green, H.W. II & Houston, H., 1995. The mechanics of deep earthquakes. *Annual Reviews of*
687 *Earth & Planetary Sciences* **23**, 169–213.
688 Green, H.W. II, Chen, W.-P. & Brudzinski, M.R., 2010. Seismic evidence of negligible water
689 carried below 400-km depth in subducting lithosphere. *Nature* **467**, 828–831.
690 Guiraud, M. & Powell, R., 2006. *P–V–T* relationships and mineral equilibria in inclusions in
691 minerals. *Earth & Planetary Science Letters* **244**, 683–694.
692 Hacker, B.R., Peacock, S.M., Abers, G.A. & Holloway, S.D., 2003. Subduction factory 2. Are
693 intermediate-depth earthquakes in subducting slabs linked to metamorphic dehydration
694 reactions?. *Journal of Geophysical Research* **108**, 2030.
695 Holland, T.J.B. & Powell, R., 2001. Calculation of phase relations involving haplogranitic melts
696 using an internally consistent thermodynamic dataset. *Journal of Petrology* **42**, 673–683.
697 Holland, T.J.B. & Powell, R., 1998. An internally consistent thermodynamic data set for phases
698 of petrological interest. *Journal of Metamorphic Geology* **16**, 309–343.
699 Holland. T.J.B., Baker, J., Powell, R., 1998. Mixing properties and activity–composition
700 relationships of chlorites in the system $MgO–FeO–Al_2O_3–SiO_2–H_2O$. *European Journal of*
701 *Mineralogy* **10**, 395–406.
702 Holland, T.J.B. & Powell, R., 2011. An improved and extended internally consistent
703 thermodynamic dataset for phases of petrological interest, involving a new equation of state
704 for solids. *Journal of Metamorphic Geology* **29**, 333–383.
705 John, T. & Schenk, V., 2006. Interrelations between intermediate-depth earthquakes and fluid
706 flow within subducting oceanic plates: constraints from eclogite facies pseudotachylytes.
707 *Geology* **34**, 557–560.
708 John, T., Gussone, N., Podladchikov, Y.Y., Bebout, B.E., Dohmen, R., Halama, R., Klemd, R.,
709 Magna, R. & Seitz, H.-M., 2012. Volcanic arcs fed by rapid pulsed fluid flow through subducting
710 slabs. *Nature Geoscience* **5**, 489–492.
711 Jung, H., Green, H.W. II & Dobrzhinetskaya, L.F., 2004. Intermediate-depth earthquake faulting
712 by dehydration embrittlement with negative volume change. *Nature* **428**, 545–549.
713 Kabir, M.F. & Takasu, A., 2010. Evidence for multiple burial–partial exhumation cycles from the
714 Onodani eclogites in the Sambagawa metamorphic belt, central shikoku, Japan. *Journal of*
715 *Metamorphic Geology* **28**, 873–893.
716 Kirby, S., Engdahl, E.R. & Denlinger, R., 1996. Intermediate-depth intraslab earthquakes and arc
717 volcanism as physical expressions of crustal and uppermost mantle metamorphism in
718 subducting slabs. In: Bebout, G.E., Scholl, D.W., Kirby, S.H. & Platt, J.P. (eds.) *Subduction: Top*
719 *to Bottom, Geophysical Monograph Series* **96**. American Geophysical Union, Washington D.C.,
720 pp. 195–214.
721 Kohn, M.J., 2014. “Thermoba-Raman-try”: calibration of spectroscopic barometers and
722 thermometers for mineral inclusions. *Earth & Planetary Science Letters* **388**, 187–196.
723 Krogh, E.J., Oh, C.W. & Liou, J.G., 1994. Polyphase and anticlockwise *P–T* evolution for
724 Franciscan eclogites and blueschists from Jenner, California, USA. *Journal of Metamorphic*
725 *Geology* **12**, 121–134.
726 Lu, R. & Keppler, H., 1997. Water solubility in pyrope to 100 kbar. *Contributions to Mineralogy*
727 *& Petrology* **129**, 35–42.

Li, J.-L., Klemd, R., Gao, J. & John, T., 2016. Poly-cyclic metamorphic evolution of eclogite: evidence of multistage burial–exhumation cycling in a subduction channel. *Journal of Petrology* **57**, 119–146.

Lister, G.S. & Forster, M.A., 2016. White mica $^{40}Ar/^{39}Ar$ age spectra and the timing of multiple episodes of high-*P* metamorphic mineral growth in the Cycladic eclogite–blueschist belt, Syros, Aegean Sea, Greece. *Journal of Metamorphic Geology* **34**, 401–421.

Meyer, M., Klemd, R., John, T., Gao, J. & Menneken, M., 2016. An (in-)coherent metamorphic evolution of high-*P* eclogites and their host rocks in Chinese southwest Tianshan?. *Journal of Metamorphic Geology* **34**, 121–146.

Monecke, K., Finger, W., Klarer, D., Kongko, W., McAdoo, B.G., Moore, A.L. & Sudrajat, S.U., 2008. A 1,000-year sediment record of tsunami recurrence in northern Sumatra. *Nature* **455**, 1234–1234.

Nakajima, J., Uchida, N., Shiina, T., Hasegawa, A., Hacker, B.R. & Kirby, S.H., 2013. Seismic evidence for reactivation of a buried hydrated fault in the Pacific slab by the 2011 M9.0 Tohoku earthquake. *Geophysical Research Letters* **38**, L00G06.

Nakajima, J., Uchida, N., Shiina, T., Hasegawa, A., Hacker, B.R. & Kirby, S.H., 2013. Intermediate-depth earthquakes facilitated by eclogitization-related stresses. *Geology* **41**, 659–662.

Nanayama, F., Satake, K., Furukawa, R., Shimokawa, K., Atwater, B.F., Shigeno, K. & Yamaki, S., 2003. Unusually large earthquakes inferred from tsunami deposits along the Kuril trench. *Nature* **424**, 660–663.

Nabelek, P.I., 2015. Hydrofracturing of sediment and hydrated MORB's during subduction of ocean crust. *American Geophysical Union Fall Meeting Abstracts***, 2015AGUFM.S34A..01N**.

Nelson, A.R., 1996. Identifying coseismic subsidence in tidal–wetland stratigraphic sequences at the Cascadia subduction zone of western North America. *Journal of Geophysical Research B* **101**, 6115–6135.

Padrón-Navarta, J.A., Sánchez-Vizcaíno, V.L., Garrido, C.J. & Gómez-Pugnaire, M.T., 2011. Metamorphic record of high-pressure dehydration of antigorite serpentinite to chlorite harzburgite in a subduction setting (Cerro del Almirez, Nevado–Filábride complex, southern Spain). *Journal of Petrology* **52**, 2047–2078.

Page, F.Z., Armstrong, L.S., Essene, E.J. & Mukasa, S.B., 2007. Prograde and retrograde history of the Junction school eclogite, California, and an evaluation of garnet–phengite–clinopyroxene thermobarometry. *Contributions to Mineralogy & Petrology* **153**, 533–555.

Page, F.Z., Mukasa, S.B., Essene, E.J. & Valley, J.W., 2014. A garnet–zircon oxygen isotope record of subduction and exhumation fluids from the Franciscan Complex, California. *Journal of Petrology* **55**, 103–131.

Powell, R. & Holland, T.J.B., 1999. Relating formulations of the thermodynamics of mineral solid solutions: activity modeling of pyroxenes, amphiboles, and micas. *American Mineralogist* **84**, 1–14.

Preston, L.A., Creager, K.C., Crosson, R.S., Brocher, T.M. & Trehu, A.M., 2003. Intraslab earthquakes: dehydration of the cascadia slab. *Science* **302**, 1197–1200.

Raimbourg, H., Goffé, B & Jolivet, L., 2007. Garnet reequilibration and growth in the eclogite facies and geodynamical evolution near peak metamorphic conditions. *Contributions to Mineralogy & Petrology* **153**, 1–28.

Rubatto, D., Regis, D., Hermann, J., Boston, K., Engi, M., Beltrando, M. & McAlpine, S.R., 2011. Yo-yo subduction recorded by accessory minerals in the Italian Western Alps. *Nature Geoscience* **4**, 338–342.

Schmidt, C. & Ziemann, M.A., 2000. In-situ Raman spectroscopy of quartz: a pressure sensor for hydrothermal diamond-anvil cell experiments at elevated temperatures. *American Mineralogist* **85**, 1725–1734.

Schubnel, A., Brunet, F., Hilairet, N., Gasc, J., Wang, Y. & Green, H.W. II, 2013. Deep-focus earthquake analogs recorded at high pressure and temperature in the laboratory. *Science* **341**, 1377–1380.

Spandler, C., Pettke, T. & Rubatto, D., 2011. Internal and external fluid sources for eclogite-facies veins in the Monviso meta-ophiolite, western Alps: implications for fluid flow in subduction zones. *Journal of Petrology* **52**, 1207–1236.

Syracuse, E.M., & Abers, G.A., 2006. Global compilation of variations in slab depth beneath arc volcanoes and implications. *Geochemistry, Geophysics, Geosystems* **7**, 5.

Taylor, F.W., 1990. Seismic recurrence intervals and timing of aseismic subduction inferred from emerged corals and reefs of the Central Vanuatu (New Hebrides) frontal arc. *Journal of Geophysical Research B* **95**, 393–408.

Tsujimori, T., Matsumoto, K., Wakabayashi, J. & Liou, J.G., 2006a. Franciscan eclogite revisited: reevaluation of the *P–T* evolution of tectonic blocks from Tiburon Peninsula, California, U.S.A. *Mineralogy & Petrology* **88**, 243–267.

Tsujimori, T., Sisson, V.B., Liou, J.G., Harlow, G.E. & Sorensen, S.S., 2006b. Petrologic characterization of Guatemalan lawsonite eclogite: eclogitization of subducted oceanic crust in a cold subduction zone. *In*: Hacker, B.R., McClelland, W.C. & Liou, J.G. (eds.) *Ultrahigh Pressure Metamorphism: Deep Continental Subduction*. *Geological Society of America Special Papers* **403**, 147–168.

Vrijmoed, J.C., Podladchikov, Y.Y., Andersen, T.B. & Hartz, E.H., 2009. An alternative model for ultra-high pressure in the Svartberget Fe–Ti garnet-peridotite, Western Gneiss Region, Norway. *European Journal of Mineralogy* **21**, 1119–1133.

Wakabayashi, J., 1990. Counterclockwise P–T–t paths from amphibolites, Franciscan Complex, California: relics from the early stages of subduction zone metamorphism. *Journal of Geology* **98**, 657–680.

Wakabayashi, J., 2012. Subducted sedimentary serpentinite mélanges: record of multiple burial–exhumation cycles and subduction erosion. *Tectonophysics* **568–569**, 230–247.

Wei, C.J. & Powell, R., 2003. Phase relations in high-pressure metapelites in the system KFMASH (K_2O–FeO–MgO–Al_2O_3–SiO_2–H_2O) with application to natural rocks. *Contributions to Mineralogy & Petrology* **145**, 301–315.

White, R.W., Powell, R., Holland, T.J.B. & Worley, B.A., 2000. The effect of TiO_2 and Fe_2O_3 on metapelitic assemblages at greenschist and amphibolite facies conditions: mineral equilibria calculations in the system K_2O–FeO–MgO–Al_2O_3–SiO_2–H_2O–TiO_2–Fe_2O_3. *Journal of Metamorphic Geology* **18**, 497–511.

White, R.W., Powell, R. & Holland, T.J.B., 2001. Calculation of partial melting equilibria in the system Na_2O–CaO–K_2O–FeO–MgO–Al_2O_3–SiO_2–H_2O (NCKFMASH). *Journal of Metamorphic Geology* **19**, 139–153.

White, R.W., Powell, R. & Phillips, G.N., 2003. A mineral equilibria study of the hydrothermal alteration in mafic greenschist facies rocks at Kalgoorlie, Western Australia. *Journal of Metamorphic Geology* **21**, 455–468.

Withers, A.C., Wood, B.J. & Carroll, M.R., 1998. The OH content of pyrope at high pressure. *Chemical Geology* **147**, 161–171.

Zhang, Y., 1998. Mechanical and phase equilibria in inclusion–host systems. *Earth & Planetary Science Letters* **157**, 209–222.

Acknowledgments

Ken Livi provided technical assistance for electron microprobe work at Johns Hopkins. Katy Chamberlain, George Cooper and Emily Finch helped with the synchrotron work. Discussions with Mike Brown helped hone the proposed model for seismicity-driven metamorphism. Andy Beeby generously provided access to the Raman Spectroscopy Laboratory at Durham University. Synchrotron FTIR work was funded by a Rapid Access beamtime award from the Diamond Light Source (#SM14590) and a Merit Access beamtime award from the Australian Synchrotron (#11167). Funding for the work was awarded from the Australian–American Fulbright Commission (Fulbright Victoria Fellowship to D.R.V.), and Durham University and Marie Curie actions of the European Union (International Junior Research Fellowship to D.R.V.). The paper benefitted greatly from the comments of five anonymous reviewers.